Deep Circulation Variability through the Eastern Subpolar North Atlantic

FEILI LI,[a] YAO FU,[b] M. SUSAN LOZIER,[b] ISABELA A. LE BRAS,[c] M. FEMKE DE JONG,[d] YUAN WANG,[a] AND ALEJANDRA SANCHEZ-FRANKS[e]

[a] *Xiamen University, Xiamen, China*
[b] *Georgia Institute of Technology, Atlanta, Georgia*
[c] *Woods Hole Oceanographic Institution, Woods Hole, Massachusetts*
[d] *Royal Netherlands Institute for Sea Research, Texel, Netherlands*
[e] *National Oceanography Centre, Southampton, United Kingdom*

(Manuscript received 15 August 2023, in final form 8 August 2024, accepted 28 August 2024)

ABSTRACT: The export of the North Atlantic Deep Water (NADW) from the subpolar North Atlantic is known to affect the variability in the lower limb of the Atlantic meridional overturning circulation (AMOC). However, the respective impact from the transport in the upper NADW (UNADW) and lower NADW (LNADW) layers, and from the various transport branches through the boundary and interior flows, on the subpolar overturning variability remains elusive. To address this, the spatiotemporal characteristics of the circulation of NADW throughout the eastern subpolar basins are examined, mainly based on the 2014–20 observations from the transatlantic Overturning in the Subpolar North Atlantic Program (OSNAP) array. It reveals that the time-mean transport within the overturning's lower limb across the eastern subpolar gyre [-13.0 ± 0.5 Sv (1 Sv $\equiv 10^6$ m^3 s^{-1})] mostly occurs in the LNADW layer (-9.4 Sv or 72% of the mean), while the lower limb variability is mainly concentrated in the UNADW layer (57% of the total variance). This analysis further demonstrates a dominant role in the lower limb variability by coherent intraseasonal changes across the region that result from a basinwide barotropic response to changing wind fields. By comparison, there is just a weak seasonal cycle in the flows along the western boundary of the basins, in response to the surface buoyancy-induced water mass transformation.

KEYWORDS: Meridional overturning circulation; Ocean dynamics; Wind; In situ oceanic observations

1. Introduction

Warm and saline Atlantic waters are transformed into colder, fresher, and denser water masses in the subpolar North Atlantic and in the Nordic seas (Johnson et al. 2019 and references therein). Subsequent to their formation, those dense waters [known as the North Atlantic Deep Water (NADW)] are exported to lower latitudes via the lower limb of the Atlantic meridional overturning circulation (AMOC), and as such, the strength of the NADW export is suggested to affect the AMOC variability and its time scales (e.g., Zou et al. 2019).

The NADW is typically decomposed into two layers: the upper NADW (UNADW) contains the deep waters formed in the Labrador and Irminger Basins (Pickart et al. 2003; Yashayaev et al. 2015; de Jong et al. 2018), while the lower NADW (LNADW) mainly contains the overflow waters from the Greenland–Scotland Ridge (GSR; Dickson and Brown 1994; Mauritzen 1996) as well as those formed through entrainment in the eastern subpolar basins (Johns et al. 2021). A majority of previous studies have shown the dominance of UNADW transport in driving the overturning changes at the subpolar and lower latitudes (e.g., Yeager and Danabsoglu 2014; Jackson et al. 2016; Petit et al. 2023). However, recent modeling studies indicate that the subpolar overturning variability on decadal and longer time scales is associated with large UNADW anomalies (Yeager et al. 2021), and it likely involves an indirect contribution through LNADW by entrainment (Böning et al. 2023). An earlier study also showed that transport in the LNADW layer has a substantial impact on the subpolar overturning variability and on that downstream (Zou et al. 2019).

Besides the transport in individual layers, the various transport branches of NADW across the subpolar region could impact the overturning there. Traditionally, the circulation of NADW has been thought to flow primarily along the deep boundary current of the subpolar basins and subsequently be exported to the lower latitudes along the deep western boundary current (McCartney 1992; Dickson and Brown 1994). However, recent Lagrangian studies have shed light on the significance of the interior transport pathways for deep-water exchanges between the subbasins of the Atlantic (e.g., Bower et al. 2019). These alternative transport pathways have an impact on the strength of NADW export from the subpolar basins at much longer time scales. For example, deep waters formed in the Labrador Sea (i.e., UNADW) primarily flow along the interior pathways and recirculate within the subpolar gyre for up to decades before getting exported to the subtropics according to eddy-permitting ocean circulation models (Gary et al. 2012; Zou and Lozier 2016). Similarly, transports of the LNADW are not restricted to the boundary currents

Denotes content that is immediately available upon publication as open access.

Supplemental information related to this paper is available at the Journals Online website: https://doi.org/10.1175/JCLI-D-23-0487.s1.

Corresponding author: Feili Li, feili.li@xmu.edu.cn

DOI: 10.1175/JCLI-D-23-0487.1

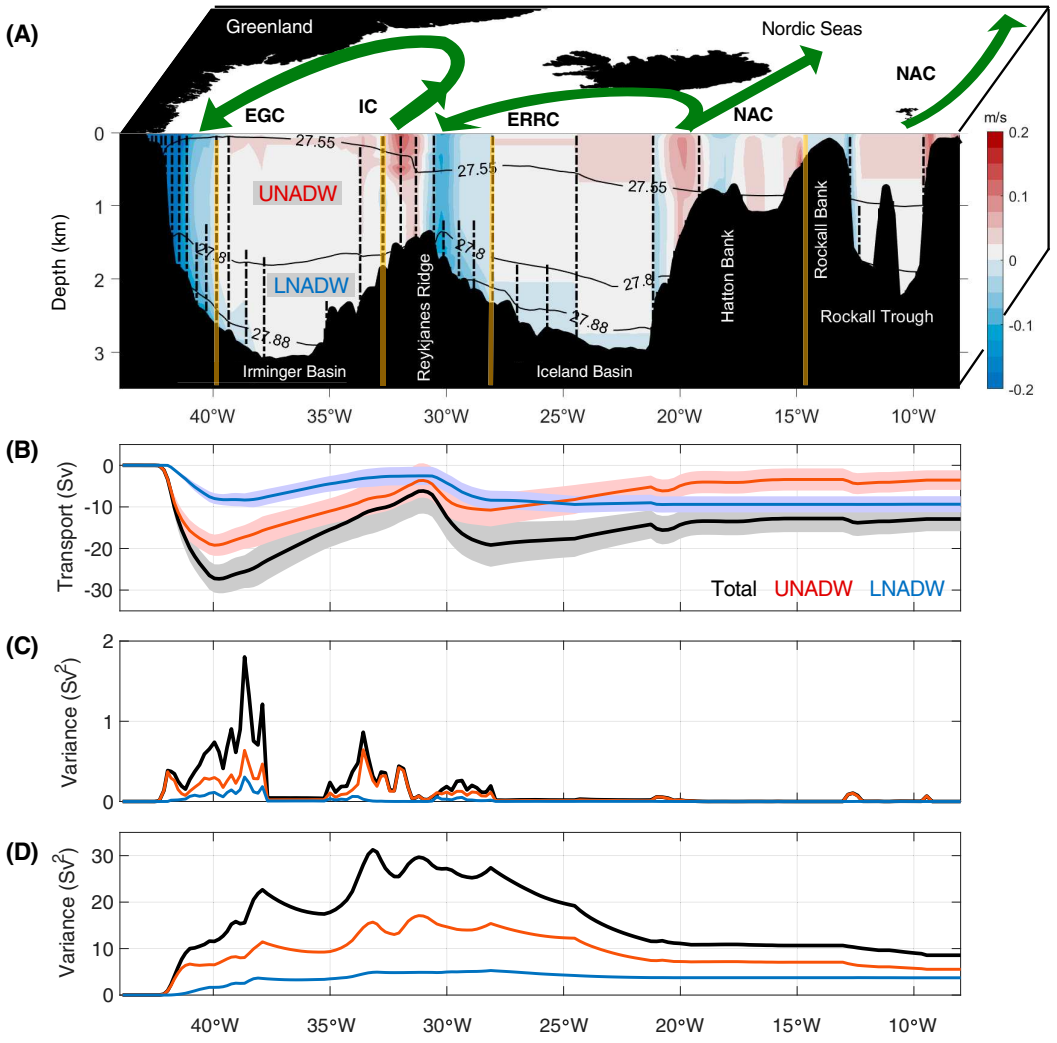

FIG. 1. (a) Schematic for mean circulations in the eastern subpolar North Atlantic basins. Color shading indicates the August 2014–June 2020 mean velocity across the OSNAP East section (at approximately 58°N), with positive values for poleward flow normal to the section. Black contours indicate isopycnals σ_θ that delimit the major water masses in the region. Vertical lines indicate the location of OSNAP moorings. Vertical yellow lines indicate the location that delimits the boundary and interior flows (see the main text for details). Green arrows indicate major boundary currents including the NAC, the East Reykjanes Ridge Current (ERRC), the Irminger Current (IC), and the Eastern Greenland Current (EGC). (b) Volume transport in the lower limb, the UNADW and LNADW layers, accumulated from west to east along the section. Shading indicates one standard deviation from the time mean. (c) The transport variance in the local transport in each layer. (d) As in (c), but in the eastward-accumulated transport.

but take multiple interior pathways both in the subpolar basin and along its equatorward export (Xu et al. 2010; Lozier et al. 2013; Zou et al. 2020; Zhai et al. 2021; Lozier et al. 2022).

While these results have brought rich insights into deep ocean circulation in the subpolar region, they raise the question as to how the overturning's lower limb variability is influenced by transports in individual NADW layers and in the boundary and interior flows. Full water column measurements from the transatlantic Overturning in the Subpolar North Atlantic Program (OSNAP) (Lozier et al. 2017) array have provided an unprecedented opportunity for addressing this question from an observational perspective. The continuous observations since 2014 show that the variability in the subpolar overturning is mainly accounted for by changes in the eastern subpolar gyre (across the OSNAP East section; Fig. 1a; Lozier et al. 2019), and it is partially attributed to anomalies along the western boundary in the Irminger Sea (Li et al. 2021). Though that study concluded that interior flows throughout the Irminger and Iceland basins needed to be included for a fuller attribution, it did not specify the relative contributions from the individual currents across the region nor did it address whether these relative contributions depend on the time scale of the variability. Such contributions likely involve changes in the horizontal circulation, e.g., as suggested

by a significant linkage between the gyre transport in the Irminger Sea and the total overturning strength at OSNAP (Sanchez-Franks et al. 2024). Nevertheless, the underlying mechanisms, especially that related to the circulation structure of NADW, remain elusive.

In this study, we aim to provide a closer look at the transport variability in the lower limb of the overturning in the eastern subpolar gyre at the observable time scales, using the latest OSNAP record that extends from August 2014 through June 2020. In particular, we will evaluate the impact on the subpolar overturning from the transport in individual NADW layers and from the boundary and interior transports. Following that, we will further underpin the possible driving mechanisms.

The paper is organized as follows. Section 2 introduces data and methods. Section 3 describes the time-mean features of the transport of the overturning's lower limb across OSNAP East, and section 4 analyzes the transport variability within the lower limb and the time scale of the variability and discusses its relations to changes in the wind and buoyancy forcing. Section 5 summarizes the paper with main conclusions.

2. Data and methods

a. OSNAP observations

We use the monthly gridded velocity, temperature, and salinity fields along the OSNAP East section for the time period from August 2014 to June 2020 (Fu et al. 2023). To obtain the cross-sectional velocity and property fields, mooring data in the boundary arrays are interpolated directly. Away from the arrays, temperature and salinity are produced via an objective analysis method based on all available in situ measurements along with the climatology; velocity is produced by combining the Ekman velocity derived from the wind stress, geostrophic velocities derived from the dynamic height moorings, and a compensation velocity that is required to ensure a net northward throughflow across the OSNAP East section. The reader is referred to Li et al. (2017), Lozier et al. (2019), and Fu et al. (2023) for details on the OSNAP calculation methods. The data were used to calculate the transport in the NADW layer across the section, which is defined as waters with potential density $\sigma_\theta > 27.55$ kg m^{-3} (i.e., the density surface delimits the upper and lower overturning limbs across OSNAP East). We further calculate transport in individual density classes contained in the lower limb, including the UNADW (with $\sigma_\theta = 27.55$–27.8 kg m^{-3}), the LNADW (with $\sigma_\theta > 27.8$ kg m^{-3}) that includes Northeast Atlantic Deep Water (NEADW, with $\sigma_\theta = 27.8$–27.88 kg m^{-3}), and the Denmark Strait Overflow Water (DSOW, with $\sigma_\theta > 27.88$ kg m^{-3}).

b. Wind data

We use a reanalysis wind product from the fifth major global reanalysis produced by the European Centre for Medium-Range Weather Forecasts (ECMWF) (ERA5; Hersbach et al. 2020). Monthly averaged wind data with a spatial resolution of 1/4° × 1/4° are available from January 1950. For our study, the monthly wind stresses from January 2014 to December 2020 were used.

c. Shallow water model

A wind-driven shallow water model (SWM) with real bathymetry is used to simulate the barotropic circulation response to the wind forcing exclusively. In this study, we use a version of the SWM that is based on the vertically averaged momentum equations (Greatbatch et al. 2010; Claus 2011; https://github.com/martinclaus/swm) and is similar to the model described in Wang et al. (2017). In the steady state, the equations governing the SWM are

$$\begin{aligned} -fv &= \frac{\overline{\tau_s^x}}{\rho_0 H} - \frac{1}{\rho_0 a\cos\theta}\frac{\partial p_b}{\partial \lambda} - \frac{ru}{H} + F_x, \\ fu &= \frac{\overline{\tau_s^y}}{\rho_0 H} - \frac{1}{\rho_0 a}\frac{\partial p_b}{\partial \theta} - \frac{rv}{H} + F_y, \\ 0 &= \frac{1}{a\cos\theta}\left(\frac{\partial Hu}{\partial \lambda} + \frac{\partial \cos\theta Hv}{\partial \theta}\right), \end{aligned} \tag{1}$$

where (u, v) are the vertically averaged velocities in the eastward and northward directions, respectively, a is the radius of the Earth, ρ_0 is the reference density, $(\overline{\tau_s^x}, \overline{\tau_s^y})$ are the monthly mean wind stress, (λ, θ) are the longitude and latitude, H is the ocean bottom depth, r is a linear bottom friction coefficient, and (F_x, F_y) denotes a horizontal Laplacian viscosity term with the lateral eddy viscosity coefficient given by A_h. It should be noted that the free surface variable in the SWM should be interpreted as the bottom pressure p_b.

The SWM uses a staggered latitude/longitude C grid with a horizontal resolution of 1/20° covering the North Atlantic from 82°W to 1°E and from 5°S to 68°N. The bottom topography is interpolated from General Bathymetric Chart of the Oceans (GEBCO) 15-arc-s product (GEBCO Compilation Group 2022). To inhibit topographic instability associated with the steep and rough topography (Killworth 1987) on the high-resolution SWM grid, a 3 × 3 running average filter is applied to smooth the interpolated bottom topography. A linear bottom friction coefficient of 10^{-3} m s^{-1} and a Laplacian horizontal viscosity coefficient of 150 m^2 s^{-1} are used in the SWM. As the study focuses on the large-scale barotropic transport in the open ocean rather than on the shelf, Hudson Strait, Davis Strait, Denmark Strait, the Faroe Bank Channels, the English Channel, and the Strait of Gibraltar are all closed in the model. The lateral boundaries of the SWM are closed as well.

The SWM is forced by the monthly ERA5 wind stresses (interpolated to the model grid) and is run till steady state for each month from January 2014 to December 2020. The monthly output of the SWM (i.e., wind-driven barotropic transport) was used in this study.

d. Water mass transformation

The rate of water mass transformation F is calculated by integrating surface density fluxes induced by air–sea buoyancy fluxes over the outcropping area of a given isopycnal σ^* as (Walin 1982; Tziperman 1986; Speer and Tziperman 1992)

$$F(\sigma^*) = \frac{1}{\Delta\sigma}\int\int\left[-\frac{\alpha}{C_p}Q + \beta\frac{S}{1-S}(E-P)\right]\prod(\sigma)dxdy, \quad (2)$$

where

$$\prod(\sigma) = \begin{cases} 1 & \text{for } |\sigma - \sigma^*| \le \dfrac{\Delta\sigma}{2}, \\ 0 & \text{elsewhere.} \end{cases} \quad (3)$$

In Eq. (2), α and β are the thermal expansion and haline contraction coefficients, respectively, C_p is the specific heat capacity of seawater, Q is the net heat flux into the ocean, and S is the surface salinity. The variables E and P are the evaporation and precipitation rates, respectively. The formula $\Delta\sigma = 0.2$ kg m^{-3} is the density bin size that the outcropping density (σ^*) represents. Positive transformation indicates the conversion of water lighter than the specified isopycnal to water denser than it.

The ERA5 surface heat and freshwater fluxes and the Roemmich–Gilson Argo Climatology monthly temperature and salinity (Roemmich and Gilson 2009) were used to calculate the water mass transformation rate in the eastern subpolar basins across the isopycnal of 27.55 kg m^{-3} for each month between January 2014 and December 2020.

e. Statistics

The uncertainty in the correlations is examined using the 95% significance level obtained as $1.96/\sqrt{N_{\text{eff}}}$. The variable N_{eff} is the effective number of degrees of freedom that takes into account autocorrelation (e.g., Dean and Dunsmuir 2016) as follows:

$$N_{\text{eff}} = N\frac{1 - r_A r_B}{1 + r_A r_B}, \quad (4)$$

where N is the number of observations and r_A and r_B are the lag 1 autoregressive autocorrelation coefficient of the two variables, respectively. All of the correlation coefficients quoted in this study are statistically significant at the 95% confidence level, unless otherwise noted.

We use the square of correlation coefficient r^2 for evaluating how much the total variance in the time series can be explained by one of its components (e.g., Thomson and Emery 2014).

3. Mean circulation in the lower limb of overturing

Across OSNAP East, the mean transport in the overturning's lower limb is −13.0 ± 0.5 Sv (1 Sv ≡ 10^6 m^3 s^{-1}) during 2014–20 (Table 1). Unless otherwise noted, the reported transports are mean plus/minus uncertainty, and negative (positive) values indicate equatorward (poleward) transport. Note that this magnitude is slightly smaller than the upper limb transport due to the existence of a net northward throughflow across OSNAP East (see Lozier et al. 2019 for details). This mean lower limb transport is mostly contained in the LNADW layer, which is −9.4 Sv for 2014–20 (72% of the total transport). The net transport in the UNADW layer is smaller, and its time mean is −3.6 Sv for 2014–20.

TABLE 1. The 2014–20 mean transport across OSNAP East and the Irminger and Iceland Basins, respectively (see Fig. 1 for locations). The values represent the mean plus/minus uncertainty. Positive (negative) values indicate poleward (equatorward) transport. All units are in Sverdrups.

	OSNAP East	Irminger Sea (45°–31°W)	Iceland Basin (31°–15°W)
Lower limb	−13.0 ± 0.5	−6.7 ± 0.7	−6.1 ± 0.6
UNADW	−3.6 ± 0.4	−4.1 ± 0.5	0.7 ± 0.5
LNADW	−9.4 ± 0.4	−2.6 ± 0.4	−6.8 ± 0.2

Those deep waters flow equatorward across the section primarily along the western boundary of the basins, while recirculating flows move poleward through the basin interior (Fig. 1b). The equatorward flow occurs in two main branches: near 40°W in the western Irminger Sea (−27 Sv) and near 28°W in the western Iceland Basin along the eastern flank of the Reykjanes Ridge (−13 Sv). The poleward recirculation in the lower limb is over the broader interior basin between 40° and 31°W in the Irminger Sea (20 Sv) and between 28° and 15°W in the Iceland Basin (7 Sv). The summation of all flows yields a net equatorward transport in the overturning's lower limb of ~6 Sv for the Irminger Basin and ~6 Sv also for the Iceland Basin (Table 1).

The individual circulations of UNADW and LNADW generally follow the above patterns, however, with different relative contributions from the two basins (Fig. 1b). There is a strong circulation of UNADW in the Irminger Sea that accounts for the majority of the lower limb transport there (an equatorward transport of −19 Sv near 40°W and a poleward recirculation of 15 Sv between 40° and 31°W). The net equatorward transport in the UNADW layer across OSNAP East primarily occurs via the pathways in the Irminger Sea (−41 Sv). By comparison, the circulation of LNADW is generally weaker across the Irminger Sea region (−2.6 Sv) and its net equatorward transport across the section occurs primarily along the western boundary of the Iceland Basin (−6.8 Sv).

Those transport estimates are consistent with other observations in the subpolar region. The transport in the LNADW layer is in line with the upstream transport in the layer across the GSR (Hansen and Østerhus 2000; Petit et al. 2020). Of the total southward flow across the GSR (−6 Sv; data from AtlantOS consortium; see Petit et al. 2020), −3 Sv is transported through the Denmark Strait, which is nearly the same as that across OSNAP East in the Irminger Sea (−2.6 Sv). However, while −3 Sv flows across the GSR through the Iceland–Faroe Ridge and the Faroe–Bank Channel, it is only half of that at OSNAP East in the Iceland Basin (−6.8 Sv). This increase is attributed to mixing within the Iceland Basin, likely from the UNADW and lighter layers (Johns et al. 2021). The transport in the UNADW layer across OSNAP East (−3.6 Sv) appears to be in line with the time-mean water mass transformation in the region between the GSR and OSNAP East induced by air–sea buoyancy fluxes (time mean

of 3.9 Sv during August 2014–June 2020; see section 2d for the calculation details). Note that this 2014–20 mean transformation estimate is smaller than previously reported estimates over the same region, e.g., a time mean of 7 Sv for August 2014–May 2016 (Petit et al. 2020) that was based on a shorter record and was biased toward winter months.

4. Circulation variability in the lower limb of overturning

a. *Total lower limb variability*

The total (UNADW and LNADW) lower limb transport across OSNAP East shows large variations during 2014–20, with a monthly standard deviation of 3 Sv that is ~20% of its magnitude. The transport variability in the lower limb shows a clear enhancement near the boundary currents compared to the basin's interior flows (Fig. 1c). In particular, the strongest transport variance occurs near the western boundary of the Irminger Sea (~42°–38°W). The second strongest transport variance occurs along the poleward-flowing boundary current in the eastern Irminger Sea (~36°–31°W). Those two boundary currents contribute to a large variance in the lower limb transport through the Irminger Sea (45°–31°W). Furthermore, the variance in the cumulative transport is enhanced in the Irminger Sea but reduced further into the Iceland Basin (Fig. 1d). That is, the variance in individual basins exceeds the variance in the two basins combined. It follows that the lower limb transports in the Irminger and Iceland Basins are strongly anticorrelated ($r = -0.8$), which is likely related to the recirculation around the Reykjanes Ridge (see Fig. 1a). Overall, the transport in the overturning's lower limb shows the largest variability in the Irminger Sea, which is partially counteracted by the flows through the Iceland Basin. We note that the variability discussed here is related to the total transport integrated over individual (boundary or interior) subsections at the OSNAP array (Fig. 1a). While the boundary transport is directly observed by the current meter array, the interior transport is based on endpoint geostrophy (see Lozier et al. 2019), which captures the variability in the total transport between dynamic height moorings but does not resolve local velocity variability. That local variability (e.g., due to mesoscale processes as observed in the interior Iceland Basin; see Fischer et al. 2018; Zhao et al. 2018; Zou et al. 2023) could be higher than that shown in Figs. 1c and 1d. We tested the impact of this missing variance by conducting an observing system simulation experiment (OSSE) with Global Seasonal Forecast System, version 5 (GloSea5), an ocean reanalysis product (e.g., Jackson et al. 2016), and found that the missing local variance barely has an impact on the variability of the subsection-integrated transport (Supplemental Information).

There are similar features for the flows in the UNADW layer across OSNAP East (Fig. 1). That is, the variability in the eastward-accumulated transport is much enhanced in the Irminger Sea and becomes reduced in the Iceland Basin. Compared to UNADW, the transport variability in the LNADW layer is consistently weaker in the region. Accordingly, the total transport in the UNADW layer exhibits large variance that is approximately 50% greater than that in the LNADW layer and explains the larger portion of the total variance in the lower limb transport (57% of the total variance; Fig. 2). Therefore, the changes within the lower limb of overturing in the subpolar basins are mainly concentrated in the UNADW layer. Overall, there is no statistically significant correlation between the transport variabilities in these two layers during the 2014–20 period.

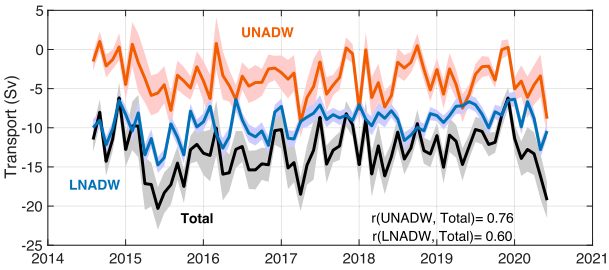

FIG. 2. Monthly time series of the volume transport in the AMOC lower limb across OSNAP East and that for UNADW and LNADW. Shading indicates uncertainty in each monthly estimate. The correlation coefficient between each deep layer transport and the total AMOC lower limb transport is shown in parentheses.

b. *Transport variability in the UNADW and LNADW layers*

We first focus on the circulation variability of UNADW in the region. Due to the zonally tilted isopycnals, the UNADW fills the upper ~2000 m of the water column in the Irminger Sea and the deeper layer between ~1000 and 2000 m in the Iceland Basin (see Fig. 1a). To separate the contribution from the various transports across the region, we divide the total transport in the UNADW layer at OSNAP East into the following geographic components: the Irminger Sea's western boundary (IRM_{wb}), its basin interior (IRM_{in}), and the eastern boundary (IRM_{eb}) and the Iceland Basin's western boundary (ICE_{wb}) and its basin interior (ICE_{in}; see Fig. 1a for locations). The transports are equatorward along the western boundaries and are poleward otherwise (Table 2).

During the time period of 2014–20, the transport in the UNADW layer exhibits changes mostly on intraseasonal (i.e., variability between a month to a year) to seasonal time scales (Fig. S1 in the online supplemental material). The intraseasonal changes consistently explain a majority of the variability in all boundary and interior flows across the region (Fig. 3), which is largest in IRM_{in} ($r^2 = 0.85$) and smallest in IRM_{wb} ($r^2 = 0.59$). By comparison, the seasonal changes contribute weakly to the total transport variability in the UNADW layer across the region ($r^2 < 0.40$). Moreover, the seasonal cycle in individual transports is not statistically significant at the 95% significance level except for the boundary currents in IRM_{wb} and ICE_{wb}.

We next examine the relationship between the UNADW transport variability and the barotropic velocity changes in individual subsections. Here, we compute a transport in the UNADW layer using the time-varying barotropic velocity and time-mean vertical area of the UNADW layer for each subsection. Given that the width of each subsection is a

TABLE 2. The 2014–20 time-mean transport in the NADW and LNADW layers across each segment across OSNAP East. The values represent the mean plus/minus uncertainty. Positive (negative) values indicate poleward (equatorward) transport. The monthly standard deviation (SD) of individual transports is also shown. All units are in Sverdrups.

	IRM_{wb}	IRM_{in}	IRM_{eb}	ICE_{wb}	ICE_{in}
UNADW	−19.2 ± 0.4	11.7 ± 0.4	3.4 ± 0.4	−6.7 ± 0.4	7.4 ± 0.5
Monthly SD	2.6	3.5	2.3	2.2	2.4
LNADW	−8.0 ± 0.4	5.2 ± 0.3	0.2 ± 0.04	−5.8 ± 0.2	−1.0 ± 0.2
Monthly SD	1.3	2.2	0.13	1.3	1.2

constant, the vertical area is proportional to the layer thickness of the respective subsections. We define the barotropic velocity as the depth-averaged velocity field and the spatial-mean layer thickness as the vertical distance between the two isopycnals defining UNADW (i.e., 27.55 and 27.80 kg m^{-3}). The results show that UNADW transport variability has strong correlations with the barotropic transport variability ($r \geq 0.74$; gray dots in Fig. 4), which is strongest for the interior flows in IRM_{in} and ICE_{in} ($r > 0.9$). It suggests that the interior transport is essentially barotropic, while the boundary transport is not. Moreover, the correlations are strengthened especially for the boundary current when only considering variability over intraseasonal time scales ($r \sim 0.9$; blue dots in Fig. 4). Therefore, the barotropic velocity is the major source of intraseasonal transport variability in the UNADW layer. By comparison, we also compute a transport in the UNADW layer using the time-varying layer thickness and the time-mean barotropic velocity for each subsection. Their correlations with the total transport in the UNADW layer are substantially weaker across OSNAP East ($r \leq 0.6$, gray dots in Fig. S2), suggesting that layer thickness anomalies play a minor role in the total transport variability in the UNADW layer.

Collectively, the transport variability in the UNADW layer across OSNAP East is dominated by intraseasonal changes in the barotropic velocity field, which are strongest in the interior flows in the Irminger and Iceland Basins. Only transport in the flows along the western boundary of the basins shows weak seasonal cycles, which could be related to UNADW thickness anomalies.

Beneath UNADW, the LNADW takes up the bottom layer of the eastern subpolar gyre (>2000 m; Fig. 1a). The transports are equatorward largely along the western boundary of

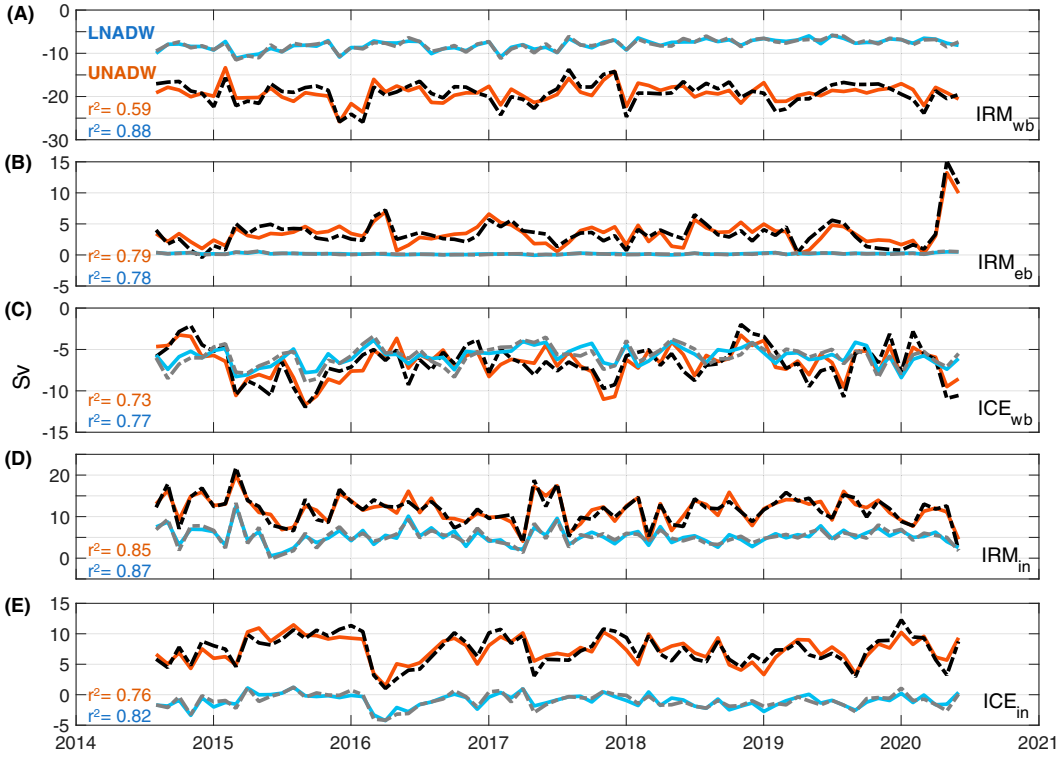

FIG. 3. (a)–(e) Monthly transport time series in the UNADW and LNADW layers (solid lines), along with the transport variability over the intraseasonal time scales (dashed lines) that is obtained by removing the monthly climatology from each monthly value. Numbers (r^2 between the solid and dashed lines) are the total transport variance explained by the intraseasonal changes for individual transports (all $p < 0.01$).

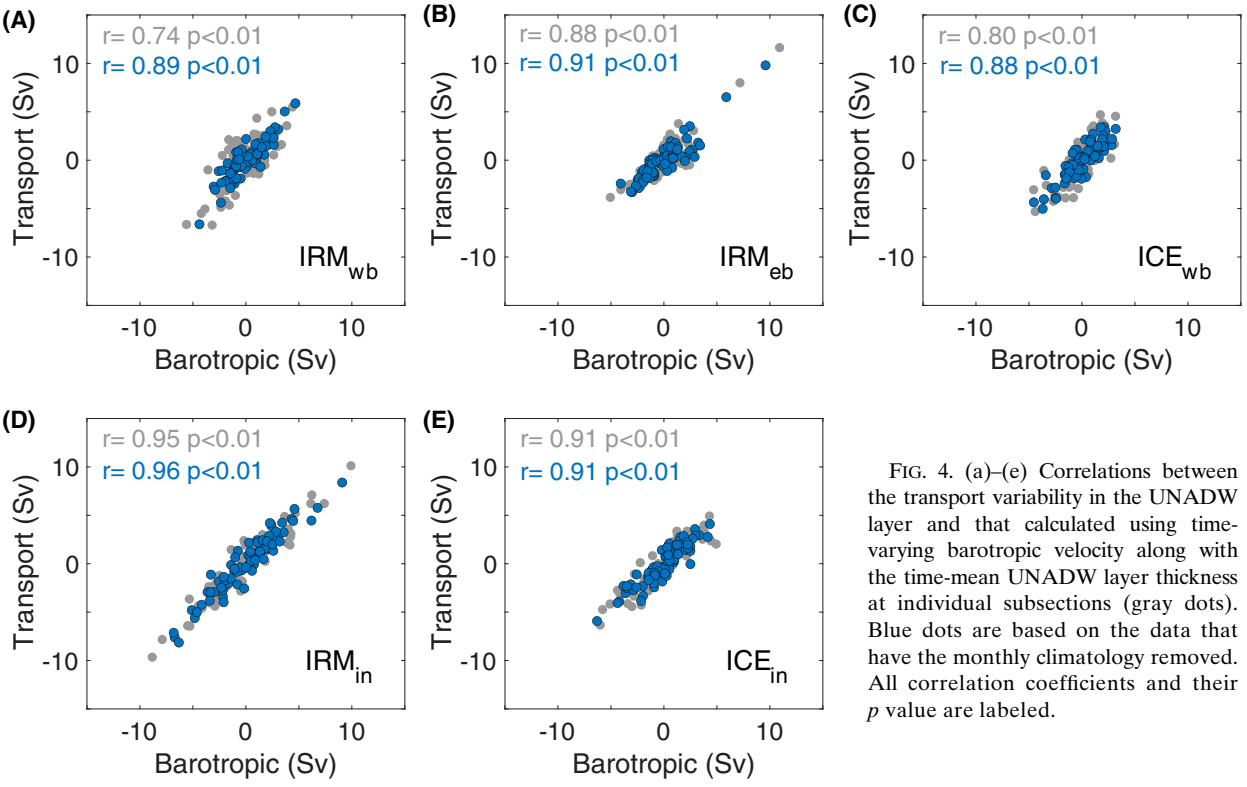

FIG. 4. (a)–(e) Correlations between the transport variability in the UNADW layer and that calculated using time-varying barotropic velocity along with the time-mean UNADW layer thickness at individual subsections (gray dots). Blue dots are based on the data that have the monthly climatology removed. All correlation coefficients and their p value are labeled.

the basins and are poleward only through the interior Irminger Sea (Table 2). During 2014–20, the transport in the LNADW layer is consistently more stable across the region than UNADW, e.g., it has a smaller standard deviation of the monthly series. This transport variability is mostly accounted for by the intraseasonal changes everywhere across the region ($r^2 \geq 0.77$, Fig. 3), which is different from UNADW that has a mixed contribution from both intraseasonal and seasonal changes.

The transport variability in the LNADW layer exhibits similarly strong correlations with the barotropic velocity changes over intraseasonal time scales (Fig. 5). However, the barotropic contribution is overall weaker than that for UNADW, particularly along the main paths for LNADW in the boundary currents ($r \sim 0.6$; gray dots in Fig. 5). This is associated with a clear impact from changes in the LNADW layer thickness (defined as the vertical distance from the isopycnal 27.80 kg m^{-3} to the sea floor) over intraseasonal time scales (r up to 0.7; blue dots in Fig. S3). Overall, the transport variability in the LNADW layer across OSNAP East is dominated by intraseasonal changes in the barotropic velocity and partly by that in LNADW thickness.

c. *Relation to the wind-driven circulation*

We next focus on the circulation variability of UNADW given the dominance of the barotropic changes across the region and evaluate the extent to which the local wind forcing impacts the variability. The dominance of the barotropic transport is consistent with the main circulation feature in the region, which is strongly barotropic/weakly baroclinic (e.g., Lavender et al. 2005; Lherminier et al. 2010) and is suggested to be mainly wind-driven (Spall and Pickart 2003). As such, the observed intraseasonal circulation variability within the overturing's lower limb may be related to the local wind forcing (e.g., Sanchez-Franks et al. 2024). This can be readily seen with the prevailing positive correlations between the transport variations through the Irminger and Iceland Basins' interior and the variations in the wind stress curl over the eastern subpolar gyre (Fig. 6a). Here, a positive correlation implies that a stronger positive wind stress curl leads to a stronger cyclonic circulation (through the conservation of potential vorticity; Gill 1982) and thus a stronger poleward transport through the interior basins. As expected, similarly strong yet negative correlations exist for the boundary transport variations (Fig. S4).

The strong linkages between the circulation of UNADW and the local wind stress curl are well preserved over the intraseasonal time scales (Fig. 6b). This is consistent with the time scale of the transport variability in the UNADW layer (section 4b). In particular, strong and positive correlations are collocated with regions showing large wind stress curl in the Irminger Sea. The correspondence indicates the role of the wind-driven circulation in the Irminger Sea for the export of UNADW via the overturning's lower limb. Indeed, the response to the wind forcing seems to mainly exist for the flows through the Irminger Sea, not through the Iceland Basin (e.g., strongest correlations with the local wind over the Irminger Sea; see Figs. 6c,d and Fig. S5).

The wind-driven circulation changes can be directly estimated based on the barotropic streamfunction obtained from

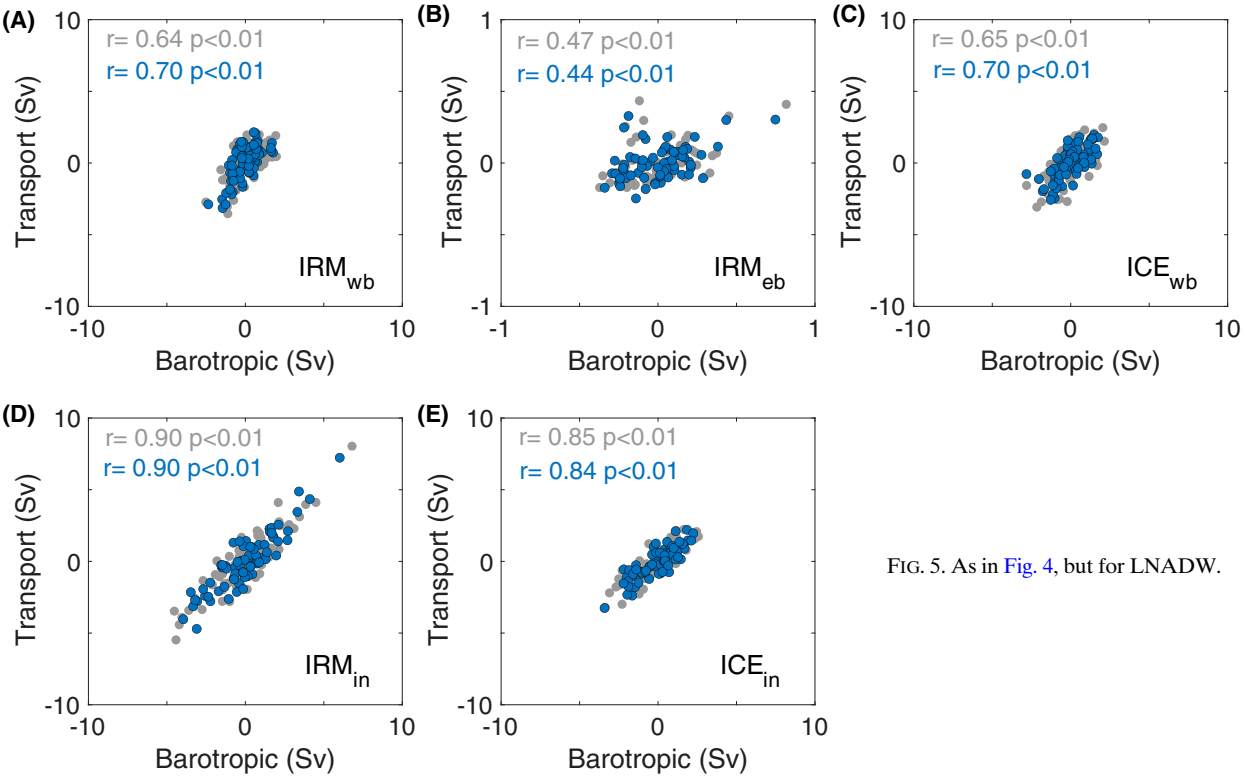

FIG. 5. As in Fig. 4, but for LNADW.

the SWM reconstruction, which well reproduces the strong cyclonic circulation that is manifested in the Irminger Sea region (Fig. 7a). During the 2014–20 time period, the circulation strength, defined as the minimum of the barotropic streamfunction, exhibits large month-to-month variations that can range from ~−11 Sv to nearly zero (monthly standard deviation of ~3 Sv), which is dominated by changes over the intraseasonal time scales (r^2 = 0.54). The changes in the wind-driven transport from the SWM through the interior of the Irminger and Iceland Basins have a significant correlation with the interior transport variations in the UNADW layer from the observations (r = 0.5, Fig. 7b). This moderate correlation can be due to the fact that the SWM-simulated barotropic circulation is exclusively wind-driven and it can be damped due to the bottom friction parameterized in the model. Furthermore, the results also indicate a leading role of the Irminger Sea barotropic circulation (light blue line; Fig. 7b), which is in line with that observed. There are similar correlations for the boundary regions between the observed transport and the wind-driven transport from the SWM (Table S1). Collectively, changing subpolar wind fields dominates the intraseasonal transport variability in the UNADW layer via the barotropic processes.

The wind forcing can also affect the strength of the horizontal circulation through its impact on the horizontal slope of the isopycnals (e.g., Fried and de Jong 2022). However, previous studies suggested that changes in the density field have an impact on the circulation variability mainly over the interannual and longer time scales (Våge et al. 2011; Wang et al. 2021; Böning et al. 2023). This at least partially explains why changes in the layer thickness do not seem to be directly linked to the transport variations in the basin interior transport from the OSNAP records.

The southward Ekman transport across OSNAP East opposes the northward transport of waters in the upper overturning limb, which is shown to affect the seasonality of the subpolar overturning circulation (Fu et al. 2023). However, there is no significant correlation between the 71-month Ekman transport and the overturning transport at OSNAP East (r = 0.2), suggesting a negligible impact from the Ekman transport on intraseasonal time scales during the 2014–20 time period.

d. Relation to the surface buoyancy-driven water mass transformation

Anomalies in the UNADW volume within the eastern subpolar basins have been linked to local buoyancy forcing during winters (de Jong et al. 2018; Petit et al. 2020). Although the buoyancy-driven transformation occurs in a progressive way as the warm surface waters propagate across the Iceland and Irminger Basins consecutively (Petit et al. 2021; Le Bras et al. 2022), the formation of UNADW in the eastern subpolar gyre mostly occurs within the Irminger Sea (~80% of the total; Fig. 8). After its formation, UNADW can be quickly exported via the western boundary current and subsequently impact the transport variability there. This impact is most prominent over the seasonal time scale. As shown in Fig. 8, strong seasonal changes in the UNADW layer thickness are observed along the basin's western boundary, with a peak in

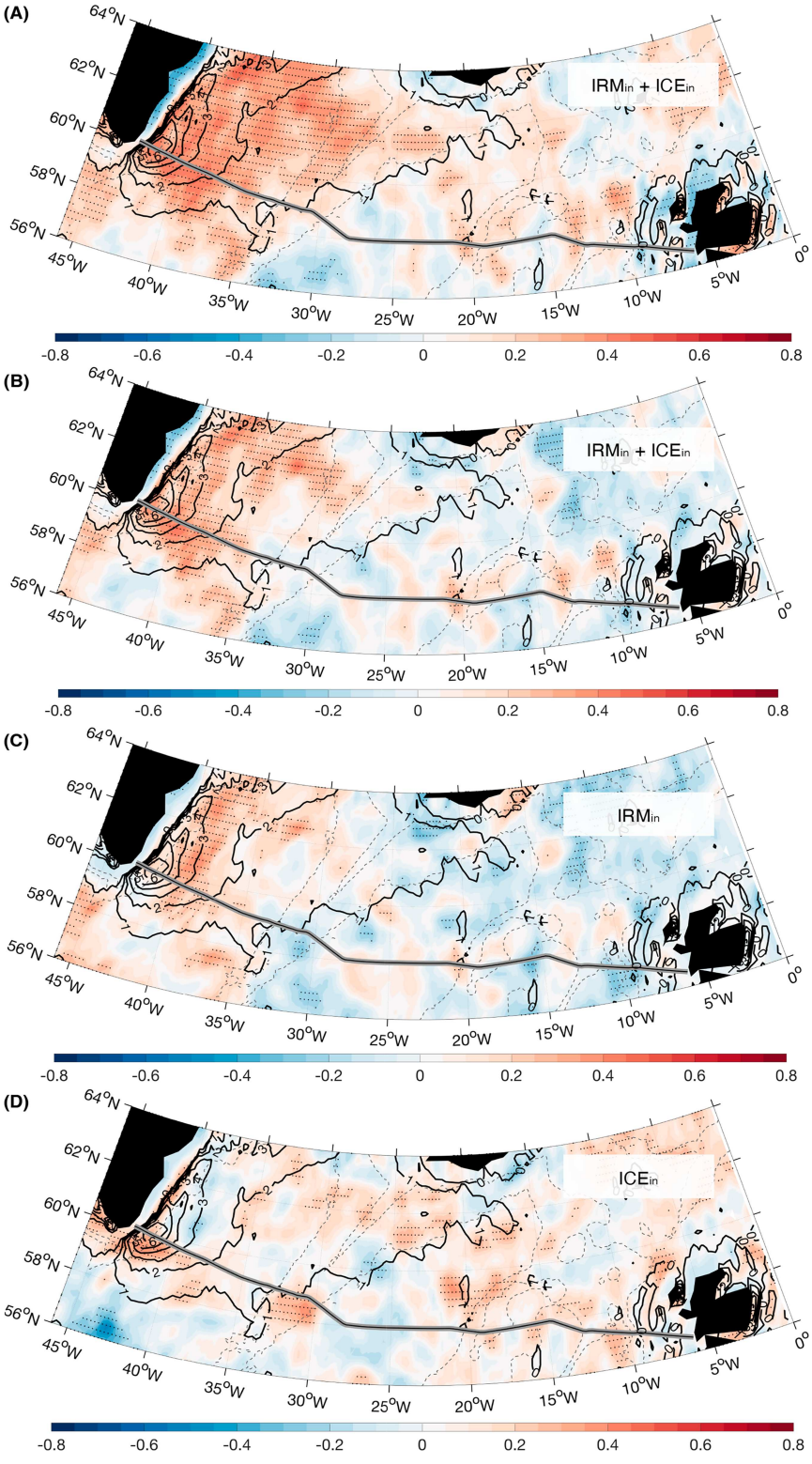

FIG. 6. (a) Correlations (color shading) between the local wind stress curl and the transport in the UNADW layer through the interior of the Irminger and Iceland Basins. Significant correlations at the 90% confidence level are stippled. All data have been linearly detrended before calculating the correlations. The 2014–20 mean wind stress curl (10^{-7} N m^{-3}) is overlaid with

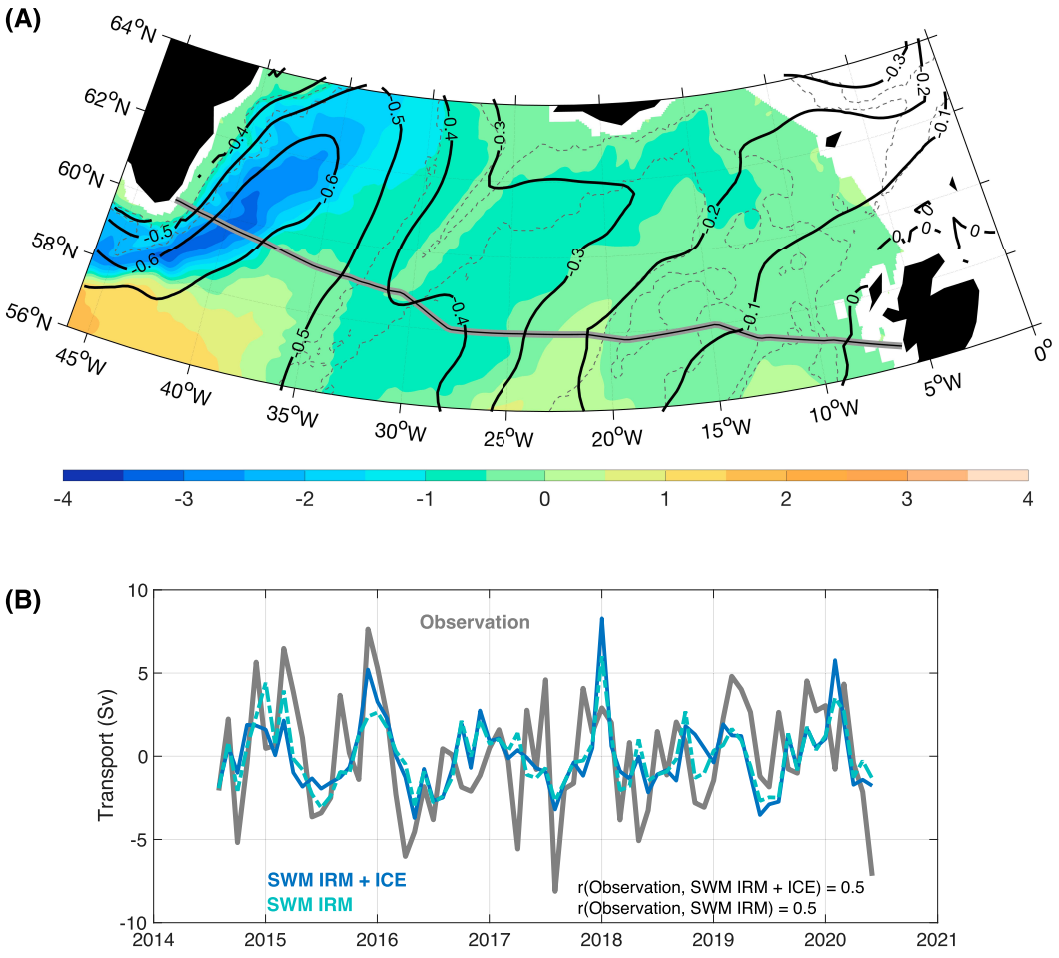

FIG. 7. (a) The 2014–20 mean barotropic streamfunction (color shading; Sv) obtained from the SWM, overlaid by the 2014–20 absolute dynamic height (ADT; black contour; m). The ADT data have been spatially smoothed with a 5° (latitude) × 10° (longitude) moving window. Dashed contours indicate the 1000- and 2000-m isobath. The thick gray line indicates the location of the OSNAP East section. (b) The monthly time series of the transport in the UNADW layer through the Irminger and Iceland Basins' interior (gray line) compared with the barotropic transport across the Irminger and Iceland Basins' interior (blue solid line) and across the Irminger Sea's interior alone (light blue dashed line) from the SWM. All the data have been linearly detrended.

January–March (JFM) that decreases throughout summer of each year. That is, the export of those thickness anomalies via the western boundary current can take up to a couple of months after their formation, e.g., depending on the formation location in the Irminger Sea (e.g., Le Bras et al. 2020; Petit et al. 2021; Fu et al. 2023). Overall, the water mass transformation in the region tends to imprint its clear seasonal signature to the boundary current transport in the UNADW layer (see Fig. S2).

It is worth noting that the seasonal transport changes in the UNADW layer, which are strongest in JFM for IRM_{wb}, lead the seasonal overturning transport changes that are strongest in April–June. Such a time lag can be attributed to the seasonal changes in the Ekman transport (strongest in JFM), which act to delay the peak overturning transport to Spring (Fu et al. 2023).

5. Discussion and conclusions

Using a 6-yr observation record from 2014 to 2020, we examine circulation characteristics within the overturning's lower limb across the eastern subpolar North Atlantic and

←

black contours (only positive curls are shown). Dashed contours indicate the 1000- and 2000-m isobath. The thick gray line indicates the location of the OSNAP East section. (b) As in (a), but using the high-pass-filtered data with a 12-month Butterworth filter. (c),(d) As in (b), but for the transport through the interior Irminger and Iceland Basins, respectively.

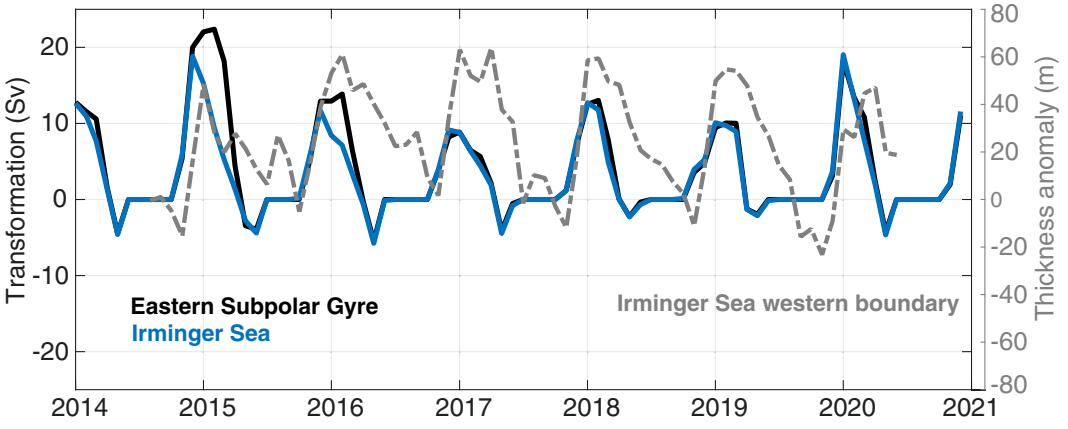

FIG. 8. Buoyancy-induced water mass transformation across isopycnal of 27.55 kg m^{-3} in the Irminger Sea (blue line; between the Greenland–Iceland–Scotland Ridge and the OSNAP line and west of the Reykjanes Ridge) and over the entire eastern subpolar gyre (between the Greenland–Iceland–Scotland Ridge and the OSNAP East line). Positive values mean lighter water being transformed to denser water. The gray dashed line indicates the observed month-to-month changes in the UNADW layer thickness along the western boundary of the Irminger Sea (right *y* axis).

evaluate the contributions from transport through various layers and locations explicitly. Over the 2014–20 period, the time-mean transport in the AMOC lower limb (i.e., in the NADW layer) is −13.0 ± 0.5 Sv across OSNAP East. While its mean is mostly accounted for by the transport in the LNADW layer (−9.4 Sv or 72% of the mean), the transport variability over the observed time scales is slightly larger in the UNADW layer (57%) compared to the LNADW layer. The circulation of UNADW in the eastern subpolar North Atlantic during 2014–20 is dominated by intraseasonal variability, following barotropic response to changes in the local wind fields. The wind-driven variability is coherent across the Irminger and Iceland Basins, and its impact is manifested for the Irminger Sea interior flows. Only the transport along the western boundary of the Irminger Sea seems to have a clear yet weak seasonal cycle, following the annual export of UNADW via the western boundary current. By comparison, the 2014–20 transports in the LNADW layer across OSNAP East show no seasonality and contain almost entirely intraseasonal variability. This variability is accounted for mainly by the barotropic velocity changes and partially by layer thickness anomalies. Overall, our results highlight the importance of all the circulation pathways in the broad region east of Greenland in capturing the overturning variability there (e.g., Li et al. 2021). Moreover, the results reveal in detail the respective contributions from changes in the boundary and interior flows to the total variability in the lower limb of overturning.

In this study, we provide observational evidence for a wind-forced component of the subpolar overturning variability that has been reproduced consistently in the ocean reanalyses (Jackson et al. 2019). Our results indicate that the local wind forcing contributes to the variability in the deep-water export from the eastern subpolar basins by modulating the strength of the recirculation of those waters. This effect from the wind is most prominent in the Irminger Sea for its prevailingly strong (positive) wind stress curl. In addition, the wind can impact the overturning variability by inducing vertical movement of isopycnals (i.e., isopycnal heaving; e.g., Zhao and Johns 2014). This mechanism seems to also occur in the eastern subpolar region, indicated by an effect on the intraseasonal variability in the LNADW layer by its layer thickness anomalies. This circulation change caused by isopycnal heaving is likely part of a coherent subpolar–subtropical overturning variability, which is established through the adiabatic redistribution of water mass between the two regions that the opposing wind stress curl forcing (Yang 2015; Han 2023). Nevertheless, how the wind forcing contributes to the subpolar overturning variability at longer time scales remains unclear. A recent adjoint study found a comparable contribution from the wind and buoyancy forcing to the subpolar overturning changes over the interannual to decadal time scales (Kostov et al. 2021). Sustained observations in the region will be the key for deciphering the entangled relationships over longer time scales.

The direct impact of the wind forcing on the variability in the overturning's lower limb found in this study has an important implication on the interaction between the horizontal gyre circulation and the deep-water export from the subpolar region. This impact appears to be largest in the Irminger Sea, which has a localized recirculation gyre within the western part of the basin that is suggested to drive the overturning transport variability (Sanchez-Franks et al. 2024). However, it should be distinguished from an impact of the large-extent subpolar gyre circulation on the upper limb of the AMOC. Modeling studies indicate that a stronger subpolar gyre circulation corresponds to a stronger overturning in the subpolar region (e.g., Zhang and Thomas 2021). The linkage mainly reflects upper limb dynamics in relation to the strength of the North Atlantic Current (NAC), which occurs over the interannual and longer time scales (Wang et al. 2021). Nevertheless, this relationship is far from certain as a negative coupling between the subpolar gyre circulation and overturning appears

to exist in the geological past (e.g., Klockmann et al. 2020). Further investigations will be needed to explore the sign of the gyre-overturning coupling and its robustness from observational records.

The demonstrated role of the wind-driven variability in the eastern subpolar basins has a limitation to the observed time scales from the 6-yr records (i.e., intraseasonal-to-seasonal variability). Over the interannual and longer time scales, the surface buoyancy forcing over the Irminger and Iceland Basins is suggested to drive the overturing variability across OSNAP East (Petit et al. 2021; Böning et al. 2023). The possible process includes a progressive transformation of surface light waters into denser waters in the lower limb, thus following an integrated contribution from water mass transformation in the Iceland and then Irminger Basins (Petit et al. 2021; Tooth et al. 2023).

It is noteworthy that the observed changes in the eastern subpolar gyre can carry signatures of the Labrador Sea, which is suggested to be a key region for decadal-to-multidecadal overturning variability (e.g., Jackson et al. 2016; Yeager et al. 2021). Previous observational studies have indicated such a spreading path through which the deep-water anomalies created in the Labrador Sea arrive in the eastern subpolar basins in <1–2 years (e.g., Yashayaev et al. 2007; Chafik et al. 2022). This can be attributed to the local recirculation that is connected through the interior Labrador and Irminger Basins (Lavender et al. 2000; Fischer et al. 2018; Zou et al. 2023). A recent modeling study shows indeed the Labrador Sea anomalies imprinting decadal density changes at the deep western boundary of the Irminger Sea and strengthening the subpolar overturning (Böning et al. 2023). Moreover, models suggest that deep changes in the eastern subpolar gyre can propagate around the boundaries of the subpolar gyre and induce overturning changes in the Labrador Sea (Menary et al. 2020) and lower latitudes (Roussenov et al. 2022; Petit et al. 2023). Future investigations will be needed to connect the deep changes in the western and eastern subpolar gyre and evaluate how it affects the variability in the subpolar overturning and over the interannual and longer time scales.

The cause and effect of NADW variability highlighted in this analysis are possibly confined to the observational period between 2014 and 2020. For example, following a period of strong atmospheric forcing in the early 1990s, large LNADW anomalies occurred in the subpolar region that propagate to the subtropics causing latitudinally coherent overturning variations (Zou et al. 2019). The occurrence of LNADW anomalies is suggested to be a result of the 1990s' excessive production of a large volume of enormously dense waters in the Labrador Sea, which entered the eastern subpolar basins and modified LNADW via mixing (Böning et al. 2023). Therefore, it is likely that the basin-scale variability is largely masked by the local effects during 2014–20. A next step to examine the interbasin connectivity and its dependence on the strength of the variability will be warranted.

Finally, we note that our study relates large-scale wind forcing in the subpolar region to variability in the integrated basin transport measured by the OSNAP array. Though the OSNAP array (by design) does not capture the small-scale velocity structure in the basin interior that has been documented in other observational studies (e.g., Fischer et al. 2018; Zhao et al. 2018; Zou et al. 2023), we are confident that the array resolves the basin-integrated transport.

Acknowledgments. F. L. acknowledges the financial support from the National Key Research and Development Program of China (Grant 2023YFF0805102). M. S. L. and Y. F. acknowledge support from NSF Grant OCE-1948335. I. L. B. and A. F. acknowledge funding from the SNAP-DRAGON project (NSF Grant OCE-2038481, NERC Grant NE/T013400/1). I. L. B. also acknowledges support from NSF Grant OCE-2122579. M. F. dJ. acknowledges the financial support by the Innovational Research Incentives Scheme of the Netherlands Organisation for Scientific Research (NWO) under Grant Agreement 016.Vidi.189.130. OSNAP data were collected and made freely available by the Overturning in the Subpolar North Atlantic Program (OSNAP) project and all the national programs that contribute to it (www.o-snap.org).

Data availability statement. The 2014–2020 OSNAP data used in this study are freely available in the SMARTech Repository (https://doi.org/10.35090/gatech/70342). The wind data are from the European Centre for Medium-Range Weather Forecasts (ECMWF) atmospheric reanalyses at https://www.ecmwf.int/en/forecasts/datasets/reanalysis-datasets/era5.

REFERENCES

Böning, C. W., P. Wagner, P. Handmann, F. U. Schwarzkopf, K. Getzlaff, and A. Biastoch, 2023: Decadal changes in Atlantic overturning due to the excessive 1990s Labrador Sea convection. *Nat. Commun.*, **14**, 4635, https://doi.org/10.1038/s41467-023-40323-9.

Bower, A., and Coauthors, 2019: Lagrangian views of the pathways of the Atlantic Meridional Overturning Circulation. *J. Geophys. Res. Oceans*, **124**, 5313–5335, https://doi.org/10.1029/2019JC015014.

Chafik, L., N. P. Holliday, S. Bacon, and T. Rossby, 2022: Irminger Sea is the center of action for subpolar AMOC variability. *Geophys. Res. Lett.*, **49**, e2022GL099133, https://doi.org/10.1029/2022GL099133.

Claus, M., 2011: The Gulf Stream Extension Region: Its dynamics and interaction with the atmosphere. Diploma thesis, Christian-Albrechts-Universität, 65 pp.

Dean, R. T., and W. T. M. Dunsmuir, 2016: Dangers and uses of cross-correlation in analyzing time series in perception, performance, movement, and neuroscience: The importance of constructing transfer function autoregressive models. *Behav. Res. Methods*, **48**, 783–802, https://doi.org/10.3758/s13428-015-0611-2.

de Jong, M. F., M. Oltmanns, J. Karstensen, and L. de Steur, 2018: Deep convection in the Irminger Sea observed with a dense mooring array. *Oceanography*, **31** (1), 50–59, https://doi.org/10.5670/oceanog.2018.109.

Dickson, R. R., and J. Brown, 1994: The production of North Atlantic Deep Water: Sources, rates, and pathways. *J. Geophys. Res.*, **99**, 12 319–12 341, https://doi.org/10.1029/94JC00530.

Fischer, J., J. Karstensen, M. Oltmanns, and S. Schmidtko, 2018: Mean circulation and EKE distribution in the Labrador Sea Water level of the subpolar North Atlantic. *Ocean Sci.*, **14**, 1167–1183, https://doi.org/10.5194/os-14-1167-2018.

Fried, N., and M. F. de Jong, 2022: The role of the Irminger Current in the Irminger Sea northward transport variability. *J. Geophys. Res. Oceans*, **127**, e2021JC018188, https://doi.org/10.1029/2021JC018188.

Fu, Y., and Coauthors, 2023: Seasonality of the Meridional Overturning Circulation in the subpolar North Atlantic. *Commun. Earth Environ.*, **4**, 181, https://doi.org/10.1038/s43247-023-00848-9.

Gary, S. F., M. S. Lozier, A. Biastoch, and C. W. Boning, 2012: Reconciling tracer and float observations of the export pathways of Labrador Sea Water. *Geophys. Res. Lett.*, **39**, L24606, https://doi.org/10.1029/2012GL053978.

GEBCO Compilation Group, 2022: GEBCO_2022 Grid. Accessed 28 June 2022, https://doi.org/10.5285/e0f0bb80-ab44-2739-e053-6c86abc0289c.

Gill, A. E., 1982: *Atmosphere–Ocean Dynamics*. Academic Press, 662 pp.

Greatbatch, R. J., X. Zhai, M. Claus, L. Czeschel, and W. Rath, 2010: Transport driven by eddy momentum fluxes in the Gulf Stream extension region. *Geophys. Res. Lett.*, **37**, L24401, https://doi.org/10.1029/2010GL045473.

Han, L., 2023: Exploring the AMOC connectivity between the RAPID and OSNAP lines with a model-based data set. *Geophys. Res. Lett.*, **50**, e2023GL105225, https://doi.org/10.1029/2023GL105225.

Hansen, B., and S. Østerhus, 2000: North Atlantic–Nordic Seas exchanges. *Prog. Oceanogr.*, **45**, 109–208, https://doi.org/10.1016/S0079-6611(99)00052-X.

Hersbach, H., and Coauthors, 2020: The ERA5 global reanalysis. *Quart. J. Roy. Meteor. Soc.*, **146**, 1999–2049, https://doi.org/10.1002/qj.3803.

Jackson, L. C., K. A. Peterson, C. D. Roberts, and R. A. Wood, 2016: Recent slowing of Atlantic overturning circulation as a recovery from earlier strengthening. *Nat. Geosci.*, **9**, 518–522, https://doi.org/10.1038/ngeo2715.

——, and Coauthors, 2019: The mean state and variability of the North Atlantic circulation: A perspective from ocean reanalyses. *J. Geophys. Res. Oceans*, **124**, 9141–9170, https://doi.org/10.1029/2019JC015210.

Johns, W. E., M. Devana, A. Houk, and S. Zou, 2021: Moored observations of the Iceland-Scotland Overflow plume along the eastern flank of the Reykjanes Ridge. *J. Geophys. Res. Oceans*, **126**, e2021JC017524, https://doi.org/10.1029/2021JC017524.

Johnson, G. C., S. G. Purkey, N. V. Zilberman, and D. Roemmich, 2019: Deep Argo quantifies bottom water warming rates in the Southwest Pacific Basin. *Geophys. Res. Lett.*, **46**, 2662–2669, https://doi.org/10.1029/2018GL081685.

Killworth, P. D., 1987: Topographic instabilities in level model OGCMs. *Ocean Modell.*, **75**, 9–12.

Klockmann, M., U. Mikolajewicz, H. Kleppin, and J. Marotzke, 2020: Coupling of the subpolar gyre and the overturning circulation during abrupt glacial climate transitions. *Geophys. Res. Lett.*, **47**, e2020GL090361, https://doi.org/10.1029/2020GL090361.

Kostov, Y., and Coauthors, 2021: Distinct sources of interannual subtropical and subpolar Atlantic overturning variability. *Nat. Geosci.*, **14**, 491–495, https://doi.org/10.1038/s41561-021-00759-4.

Lavender, K. L., R. E. Davis, and W. B. Owens, 2000: Mid-depth recirculation observed in the interior Labrador and Irminger seas by direct velocity measurements. *Nature*, **407**, 66–69, https://doi.org/10.1038/35024048.

——, W. B. Owens, and R. E. Davis, 2005: The mid-depth circulation of the subpolar North Atlantic Ocean as measured by subsurface floats. *Deep-Sea Res. I*, **52**, 767–785, https://doi.org/10.1016/j.dsr.2004.12.007.

Le Bras, I. A.-A., F. Straneo, J. Holte, M. F. de Jong, and N. P. Holliday, 2020: Rapid export of waters formed by convection near the Irminger Sea's western boundary. *Geophys. Res. Lett.*, **47**, e2019GL085989, https://doi.org/10.1029/2019GL085989.

——, J. Callies, F. Straneo, T. C. Biló, J. Holte, and H.L. Johnson, 2022: Slantwise convection in the Irminger Sea. *J. Geophys. Res. Oceans*, **127**, e2022JC019071, https://doi.org/10.1029/2022JC019071.

Lherminier, P., H. Mercier, T. Huck, C. Gourcuff, F. F. Perez, P. Morin, A. Sarafanov, and A. Falina, 2010: The Atlantic Meridional Overturning Circulation and the subpolar gyre observed at the A25-OVIDE section in June 2002 and 2004. *Deep-Sea Res. I*, **57**, 1374–1391, https://doi.org/10.1016/j.dsr.2010.07.009.

Li, F., M. S. Lozier, and W. E. Johns, 2017: Calculating the meridional volume, heat, and freshwater transports from an observing system in the subpolar North Atlantic: Observing system simulation experiment. *J. Atmos. Oceanic Technol.*, **34**, 1483–1500, https://doi.org/10.1175/JTECH-D-16-0247.1.

——, and Coauthors, 2021: Subpolar North Atlantic western boundary density anomalies and the Meridional Overturning Circulation. *Nat. Commun.*, **12**, 3002, https://doi.org/10.1038/s41467-021-23350-2.

Lozier, M. S., S. F. Gary, and A. S. Bower, 2013: Simulated pathways of the overflow waters in the North Atlantic: Subpolar to subtropical export. *Deep-Sea Res. II*, **85**, 147–153, https://doi.org/10.1016/j.dsr2.2012.07.037.

——, and Coauthors, 2017: Overturning in the Subpolar North Atlantic Program: A new international ocean observing system. *Bull. Amer. Meteor. Soc.*, **98**, 737–752, https://doi.org/10.1175/BAMS-D-16-0057.1.

——, and Coauthors, 2019: A sea change in our view of overturning in the subpolar North Atlantic. *Science*, **363**, 516–521, https://doi.org/10.1126/science.aau6592.

——, A. S. Bower, H. H. Furey, K. L. Drouin, X. Xu, and S. Zou, 2022: Overflow water pathways in the North Atlantic. *Prog. Oceanogr.*, **208**, 102874, https://doi.org/10.1016/j.pocean.2022.102874.

Mauritzen, C., 1996: Production of dense overflow waters feeding the North Atlantic across the Greenland-Scotland Ridge. Part 2: An inverse model. *Deep-Sea Res. I*, **43**, 807–835, https://doi.org/10.1016/0967-0637(96)00038-6.

McCartney, M. S., 1992: Recirculating components to the deep boundary current of the northern North Atlantic. *Prog. Oceanogr.*, **29**, 283–383, https://doi.org/10.1016/0079-6611(92)90006-L.

Menary, M. B., L. C. Jackson, and M. S. Lozier, 2020: Reconciling the relationship between the AMOC and Labrador Sea in OSNAP observations and climate models. *Geophys. Res. Lett.*, **47**, e2020GL089793, https://doi.org/10.1029/2020GL089793.

Pickart, R. S., F. Straneo, G. W. K. Moore, 2003: Is Labrador Sea Water formed in the Irminger basin? *Deep-Sea Res.*I, **50**, 23–52, https://doi.org/10.1016/S0967-0637(02)00134-6.

Petit, T., M. S. Lozier, S. A. Josey, and S. A. Cunningham, 2020: Atlantic deep water formation occurs primarily in the Iceland basin and Irminger Sea by local buoyancy forcing. *Geophys.*

Res. Lett., **47**, e2020GL091028, https://doi.org/10.1029/2020GL091028.

——, ——, ——, and ——, 2021: Role of air–sea fluxes and ocean surface density in the production of deep waters in the eastern subpolar gyre of the North Atlantic. *Ocean Sci.*, **17**, 1353–1365, https://doi.org/10.5194/os-17-1353-2021.

——, ——, S. Rühs, P. Handmann, and A. Biastoch, 2023: Propagation and transformation of upper North Atlantic Deep Water from the subpolar gyre to 26.5°N. *J. Geophys. Res. Oceans*, **128**, e2023JC019726, https://doi.org/10.1029/2023JC019726.

Roemmich, D., and J. Gilson, 2009: The 2004–2008 mean and annual cycle of temperature, salinity, and steric height in the global ocean from the Argo Program. *Prog. Oceanogr.*, **82**, 81–100, https://doi.org/10.1016/j.pocean.2009.03.004.

Roussenov, V. M., R. G. Williams, M. S. Lozier, N. P. Holliday, and D. M. Smith, 2022: Historical reconstruction of subpolar North Atlantic overturning and its relationship to density. *J. Geophys. Res. Oceans*, **127**, e2021JC017732, https://doi.org/10.1029/2021JC017732.

Sanchez-Franks, A., and Coauthors, 2024: The Irminger Gyre as a key driver of the Subpolar North Atlantic Overturning. *Geophys. Res. Lett.*, **51**, e2024GL108457, https://doi.org/10.1029/2024GL108457.

Spall, M. A., and R. S. Pickart, 2003: Wind-driven recirculations and exchange in the Labrador and Irminger Seas. *J. Phys. Oceanogr.*, **33**, 1829–1845, https://doi.org/10.1175/2384.1.

Speer, K., and E. Tziperman, 1992: Rates of water mass formation in the North Atlantic Ocean. *J. Phys. Oceanogr.*, **22**, 93–104, https://doi.org/10.1175/1520-0485(1992)022<0093:ROWMFI>2.0.CO;2.

Thomson, R. E., and W. J. Emery, 2014: *Data Analysis Methods in Physical Oceanography*. 3rd ed. Elsevier Science, 728 pp.

Tooth, O. J., H. L. Johnson, and C. Wilson, 2023: Lagrangian overturning pathways in the eastern subpolar North Atlantic. *J. Climate*, **36**, 823–844, https://doi.org/10.1175/JCLI-D-21-0985.1.

Tziperman, E., 1986: On the role of interior mixing and air-sea fluxes in determining the stratification and circulation of the oceans. *J. Phys. Oceanogr.*, **16**, 680–693, https://doi.org/10.1175/1520-0485(1986)016<0680:OTROIM>2.0.CO;2.

Våge, K., and Coauthors, 2011: The Irminger Gyre: Circulation, convection, and interannual variability. *Deep-Sea Res. I*, **58**, 590–614, https://doi.org/10.1016/j.dsr.2011.03.001.

Walin, G., 1982: On the relation between sea-surface heat flow and thermal circulation in the ocean. *Tellus*, **34A**, 187–195, https://doi.org/10.3402/tellusa.v34i2.10801.

Wang, H., J. Zhao, F. Li, and X. Lin, 2021: Seasonal and interannual variability of the Meridional Overturning Circulation in the subpolar North Atlantic diagnosed from a high resolution reanalysis data set. *J. Geophys. Res. Oceans*, **126**, e2020JC017130, https://doi.org/10.1029/2020JC017130.

Wang, Y., M. Claus, R. J. Greatbatch, and J. Sheng, 2017: Decomposition of the mean barotropic transport in a high-resolution model of the North Atlantic Ocean. *Geophys. Res. Lett.*, **44**, 11 537–11 546, https://doi.org/10.1002/2017GL074825.

Xu, X., W. J. Schmitz Jr., H. E. Hurlburt, P. J. Hogan, and E. P. Chassignet, 2010: Transport of Nordic Seas overflow water into and within the Irminger Sea: An eddy-resolving simulation and observations. *J. Geophys. Res.*, **115**, C12048, https://doi.org/10.1029/2010JC006351.

Yang, J., 2015: Local and remote wind stress forcing of the seasonal variability of the Atlantic Meridional Overturning Circulation (AMOC) transport at 26.5°N. *J. Geophys. Res. Oceans*, **120**, 2488–2503, https://doi.org/10.1002/2014JC010317.

Yashayaev, I., M. Bersch, and H. M. van Aken, 2007: Spreading of the Labrador Sea Water to the Irminger and Iceland basins. *Geophys. Res. Lett.*, **34**, L10602, https://doi.org/10.1029/2006GL028999.

——, D. Seidov, and E. Demirov, 2015: A new collective view of oceanography of the Arctic and North Atlantic basins. *Prog. Oceanogr.*, **132**, 1–21, https://doi.org/10.1016/j.pocean.2014.12.012.

Yeager, S., and G. Danabasoglu, 2014: The origins of late-twentieth-century variations in the large-scale North Atlantic circulation. *J. Climate*, **27**, 3222–3247, https://doi.org/10.1175/JCLI-D-13-00125.1.

——, and Coauthors, 2021: An outsized role for the Labrador Sea in the multidecadal variability of the Atlantic overturning circulation. *Sci. Adv.*, **7**, eabh3592, https://doi.org/10.1126/sciadv.abh3592.

Zhai, Y., J. Yang, X. Wan, and S. Zou, 2021: The eastern Atlantic basin pathway for the export of the North Atlantic deep waters. *Geophys. Res. Lett.*, **48**, e2021GL095615, https://doi.org/10.1029/2021GL095615.

Zhang, R., and M. Thomas, 2021: Horizontal circulation across density surfaces contributes substantially to the long-term mean Northern Atlantic meridional Overturning Circulation. *Commun. Earth Environ.*, **2**, 112, https://doi.org/10.1038/s43247-021-00182-y.

Zhao, J., and W. E. Johns, 2014: Wind-forced interannual variability of the Atlantic Meridional Overturning Circulation at 26.5°N. *J. Geophys. Res. Oceans*, **119**, 2403–2419, https://doi.org/10.1002/2013JC009407.

——, A. Bower, J. Yang, X. Lin, and N. P. Holliday, 2018: Meridional heat transport variability induced by mesoscale processes in the subpolar North Atlantic. *Nat. Commun.*, **9**, 1124, https://doi.org/10.1038/s41467-018-03134-x.

Zou, S., and M. S. Lozier, 2016: Breaking the linkage between Labrador Sea Water production and its advective export to the subtropical gyre. *J. Phys. Oceanogr.*, **46**, 2169–2182, https://doi.org/10.1175/JPO-D-15-0210.1.

——, ——, and M. Buckley, 2019: How is meridional coherence maintained in the lower limb of the Atlantic Meridional Overturning Circulation? *Geophys. Res. Lett.*, **46**, 244–252, https://doi.org/10.1029/2018GL080958.

——, A. Bower, H. Furey, M. S. Lozier, and X. B. Xu, 2020: Redrawing the Iceland–Scotland overflow water pathways in the North Atlantic. *Nat. Commun.*, **11**, 1890, https://doi.org/10.1038/s41467-020-15513-4.

——, A. S. Bower, M. S. Lozier, and H. H. Furey, 2023: Deep ocean circulation in the subpolar North Atlantic observed by acoustically-tracked floats. *Prog. Oceanogr.*, **211**, 102975, https://doi.org/10.1016/j.pocean.2023.102975.